Available online at www.sciencedirect.com
ScienceDirect
Journal of Nuclear Materials 375 (2008) 388–396
journal of nuclear materials
www.elsevier.com/locate/jnucmat

Thermal transport properties of uranium dioxide by molecular dynamics simulations

Taku Watanabe [a], Susan B. Sinnott [a], James S. Tulenko [b], Robin W. Grimes [c], Patrick K. Schelling [d], Simon R. Phillpot [a,*]

[a] Department of Materials Science and Engineering, University of Florida, Gainesville, FL 32611, United States
[b] Department of Nuclear and Radiological Engineering, University of Florida, Gainesville, FL 32611, United States
[c] Department of Materials, Imperial College London, London SW7 2AZ, United Kingdom
[d] AMPAC and Department of Physics, University of Central Florida, Orlando, FL 32816, United States

Received 17 January 2008; accepted 24 January 2008

Abstract

The thermal conductivities of single crystal and polycrystalline UO_2 are calculated using molecular dynamics simulations, with interatomic interactions described by two different potential models. For single crystals, the calculated thermal conductivities are found to be strongly dependent on the size of the simulation cell. However, a scaling analysis shows that the two models predict essentially identical values for the thermal conductivity for infinite system sizes. By contrast, simulations with the two potentials for identical fine polycrystalline structures yield estimated thermal conductivities that differ by a factor of two. We analyze the origin of this difference.

PACS: 61.72.Mm; 65.40.−b

1. Introduction

Uranium dioxide, UO_2, is the most commonly used nuclear reactor fuel [1] and has been studied extensively for over half a century [2]. One of the most important performance metrics for nuclear fuel materials is thermal conductivity. In electronic insulators such as UO_2, thermal transport is determined by the dynamics of atomic vibrations. In crystalline materials, these vibrations are often described in terms of phonons, with their mean free path determining the thermal transport properties; there have been a number of atomic level simulations of the thermal transport properties of such materials [3–6].

While an understanding of phonon transport through a perfect lattice is important, thermal transport is often limited by accumulated defects, particularly grain boundaries. Molecular dynamics (MD) simulation methods can simulate fairly large structures, which are necessary for materials with defects. In this paper, the temperature dependence of the thermal conductivity of both single crystal and fine-grained polycrystalline UO_2 have been determined using two different descriptions of the interatomic interactions.

2. MD simulation of UO_2

2.1. Potential models

The interatomic interactions consist of a long-range electrostatic component and short-range interactions which describe the materials specific largely-repulsive component. In this work, we compare results obtained from two independent short-range interaction models: the previously published potential by Yamada et al. [7] and the Busker potential [8,9]. The Busker potential [8,9] is a traditional Buckingham potential, which is the most commonly used interaction model for ionic materials

* Corresponding author.
E-mail address: sphil@mse.ufl.edu (S.R. Phillpot).

0022-3115/$ - see front matter © 2008 Elsevier B.V. All rights reserved.
doi:10.1016/j.jnucmat.2008.01.016

Table 1
Parameters of interatomic potentials

	Busker			Yamada		
	U–U	O–O	U–O	U–U	O–O	U–O
A_{ij} [eV]	0	1761.78	9547.96	442.20	2346.15	1018.57
ρ_{ij} [nm]	0	0.03564	0.02192	0.03200	0.03200	0.03200
C_{ij} [$\times 10^{-6}$ eV nm^6]	0	0	32.00	0	4.1462	0
D_{ij} [eV]	–	–	–	0	0	0.7810
β_{ij} [1/nm]	–	–	–	0	0	12.50
r^*_{ij} [nm]	–	–	–	0	0	0.2369
Z_U [e]		+4			+2.4	
Z_O [e]		−2			−1.2	

$$\phi(r_{ij}) = A_{ij}\exp(-r_{ij}/\rho_{ij}) - \frac{c_{ij}}{r_{ij}^6}. \quad (1)$$

Here r_{ij} is the interatomic distance between atom i and j. A_{ij}, ρ_{ij}, and c_{ij} are the fitting parameters between each atomic species. The values of the parameters are given in Table 1.

One of the advantages of Busker model is the transferability of the potential between a variety of elements [8,9] – it also has parameters for U^{3+} and U^{5+}, thereby allowing the effects of off-stoichiometry to be studied. By contrast, the Yamada model is a Bushing-Ida type potential [10] given by

$$\phi(r_{ij}) = A_{ij}\exp(-r_{ij}/\rho_{ij}) - \frac{c_{ij}}{r_{ij}^6} + D_{ij}\left[\exp\left(-2\beta_{ij}(r_{ij}-r^*_{ij})\right) - 2\exp(-\beta_{ij}(r_{ij}-r^*))\right]. \quad (2)$$

The first two terms are the Buckingham potential. The last two terms are the Morse term, which provides a 'covalent' component. However, this term is not strictly covalent in the sense that it does not have directionality. Due to the assumption of partial covalency, the charges of the ions are given by non-formal values intended to represent the partial charge transfer between ions (see Table 1).

To avoid the prohibitive computational expense associated with the Ewald method [11], particularly for systems with large numbers of ions, the electrostatic interactions are calculated using the direct-summation method [12]. The direct-summation technique involves truncation of the electrostatic force at a fixed cutoff radius, with charge compensation on the surface of the truncation sphere. The method has been demonstrated to be accurate and has been successfully applied to a number of materials [5,12]. It is also computationally very efficient, straightforward to implement, and has a computational load that scales linearly with system size. We established its appropriateness for these simulations through direct comparisons of Ewald and direct-summation simulations.

Table 2 summarizes the structural parameters and elastic properties determined using the two potentials. By construction, both give good values for the lattice parameters.

Table 2
Lattice parameter and elastic constants at 300 K

	GULP		MD		Experiment [17,35–38]
	Busker	Yamada	Busker	Yamada	
a [nm]	0.5481	0.5482	0.5479	0.5481	0.5478
C_{11} [GPa]	526	409	547	418	389–396
C_{12} [GPa]	118	55.0	–	–	119–121
C_{44} [GPa]	118	53.4	–	–	59.7–64.1
B [GPa]	257	174	–	–	209–213

We have used the General Utility Lattice Program (GULP) [13,14] to determine the elastic properties at 300 K. GULP uses a static method based on the quasi-harmonic approximation and thus provides slightly lower estimated values for C_{11} than does direct MD simulation, which includes the dynamical motion of the ions. We can see that while the Busker potential reproduces the value of C_{12} rather well, it overestimates C_{11} and C_{44}. By contrast, the Yamada potential gives good estimates of C_{11} and C_{44}, but severely underestimates C_{12}. As a result one overestimates and the other underestimates the bulk modulus $B = (C_{11} + 2C_{12})/3$.

Recently, Govers et al. undertook an extensive comparison of a number of empirical potentials for UO_2, including the two used in this study [15]. Their assessment included both rigid-ion and shell models, and they calculated cohesive energies, lattice parameters, elastic constants, dielectric constants, Γ point phonon frequencies, and defect formation energies. While some potentials seemed to give a better physical description than others, their results show that no single potential faithfully reproduces all of the physical properties of UO_2. The two potentials used in here are thus representative of other UO_2 potentials with regards to their materials fidelity.

2.2. Thermal expansion

Another metric of the fidelity of the potential is to compare the thermal expansion of the system with experiment. The simulations to determine the thermal expansion were performed using Andersen's constant pressure scheme [16]. The simulation cell contains $6 \times 6 \times 6$ unit cells (2592 atoms), and the temperature of the system is controlled by velocity rescaling. In order to reach equilibrium, the simulations are run for 7.5 ps with 0.25 fs time steps. The temperature is varied from 0 K to 2000 K at 100 K intervals. The lattice parameter at each temperature is obtained by the simulation cell volume average of the last 5.5 ps of the simulation.

Fig. 1 shows the normalized lattice parameter as a function of temperature; the experimental values are taken from Fink's critical assessment of the experimental data [17]. Yamada's potential shows good agreement with the experimental thermal expansion up to about 1000 K, above which it is systematically lower. The Busker potential gives a systematically lower thermal expansion at all temperatures. At low temperatures, the thermal expansions are essentially

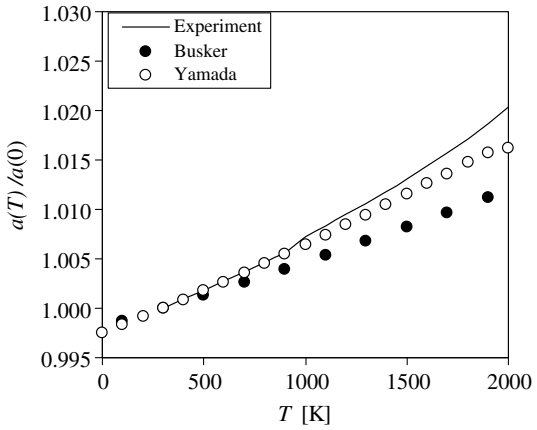

Fig. 1. Normalized lattice parameter of UO_2 from experiment and from MD simulation with the Busker and Yamada potentials. The small jog in the experimental fit is a result of different recommended data fits below and above 923 K.

temperature independent with $\alpha_{\text{Yamada}} = 8.4 \times 10^{-6}\,\text{K}^{-1}$ and $\alpha_{\text{Busker}} = 6.2 \times 10^{-6}\,\text{K}^{-1}$. The discrepancy between our calculated value for the Yamada potential and the previously published value of $10.1 \times 10^{-6}\,\text{K}^{-1}$ [7] is most likely due to the Wigner–Kirkwood correction to the free energy used in analyzing their simulations. The thermal expansion calculated with the two potentials are both smaller than the experimental value of $\alpha_{\text{Expt}} = 11.8 \times 10^{-6}\,\text{K}^{-1}$.

The thermal expansion coefficient is a result of the anharmonicity of the interactions in the material. This is encapsulated in the Grüneisen relation

$$\alpha = \frac{\gamma C_v}{3B}, \tag{3}$$

where C_v and B are the specific heat and bulk modulus, respectively, and γ is the Grüneisen parameter, which measures the dependence of the phonon frequencies on system volume, and thus the system's anharmonicity [18]. If the interatomic interactions were purely harmonic, then the Grüneisen parameter would be zero and there would be no thermal expansion. We thus interpret the higher thermal expansion of the Yamada model to be a result of higher anharmonicity in the potential.

The lattice thermal conductivity of any material is finite because of the anharmonicity of the interatomic interactions that couple the harmonic phonons to each other. Anharmonicity results in phonon scattering events, with the *Umklapp* processes producing a dissipation mechanism for energy transport [18–20].

An estimate of the lattice thermal conductivity in terms of the Grüneisen parameter was first given by Leibfried and Schloemann [21] and refined by Klemens [22],

$$\kappa \sim \frac{24}{10}\frac{\sqrt{4}}{\gamma^2}\left(\frac{k_B}{h}\right)^3 Mv\frac{\theta^3}{T}. \tag{4}$$

Here k_B is the Boltzmann constant, h is the Planck constant, v and M are the volume and the mass per atom. The only two materials constants that enter into Eq. (4) are θ, the Debye temperature, and γ the frequency-averaged Grüneisen parameter. From this relation, it is clear that the thermal conductivity decreases with increasing anharmonicity.

Through their dependences on the Grüneisen parameter, we can use Eqs. (3) and (4) to give a simple relationship between the thermal conductivity and thermal expansion, in terms of the Debye temperature, the bulk modulus and the specific heat

$$\alpha^2\kappa = \chi\frac{\theta^3 c_v^2}{B}. \tag{5}$$

The constant χ subsumes all of the non-materials constants in Eqs. (3) and (4). In classical simulations at temperatures above the Debye temperature (380–500 K for UO_2 [23,24]), such as we are performing here, the specific heat is essentially equal to the Dulong–Petit value of $3k_B$. Also we can assume that the Debye temperatures for the two potentials are the same. Hence we find

$$\kappa = \frac{\chi'}{\alpha^2 B}, \tag{6}$$

where $\chi' = \chi\theta^3 c_v^2$.

Using the values of α and B determined above for the two potentials, we then predict

$$\begin{aligned}\kappa_{\text{Busker}} &\sim 10.1 \times 10^{-2}\chi',\\ \kappa_{\text{Yamada}} &\sim 8.1 \times 10^{-2}\chi'.\end{aligned} \tag{7}$$

Using the experimental values of B and α, Eq. (6) gives $\kappa_{\text{Expt}} \sim 3.4 \times 10^{-2}\chi'$, which is considerably smaller than the predictions for the Busker and Yamada potentials. Thus, based on this very naïve analysis, we expect the direct simulations with the two potentials to give thermal conductivities for the Busker and Yamada potentials that are 3.0 and 2.4 times larger, respectively, than the experimental values; as we shall see in the next section, these estimates are quite accurate.

3. Thermal conductivity of single-crystal UO_2

The temperature dependence of the thermal conductivity of single-crystal UO_2 is calculated using the direct method [3,25]. In this approach a heat current is set up; the resulting temperature gradient is identified from which the thermal conductivity is calculated from Fourier's law.

The simulation cell is a square cylinder, long in z direction, and narrow in x and y directions: see Fig. 2. Prior to the thermal-transport simulation, the system is heated to the temperature of interest using a constant temperature, constant pressure simulation algorithm and allowed to evolve for 12.5 ps, which is sufficient for thermal and strain equilibration. The simulation cell dimensions are then fixed, and the heat source and heat sink are turned on to create a steady-state heat flow. Once the system reaches steady-state, which takes about ~500 ps, the temperature gradient is determined from an average over 250 ps, and

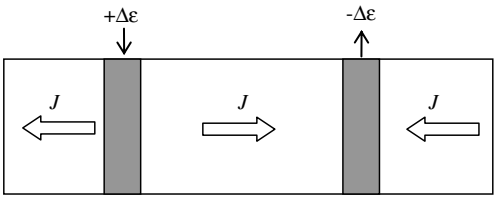

Fig. 2. Simulation cell setup for the direct method for simulating thermal conductivity. The heat source and sink are located at a quarter of the cell length away from the center of the cell. The same amount of energy, $\Delta\varepsilon$, is added to the atoms in the heat source, and removed from those in the heat sink. This setup results in two equivalent heat currents J in opposite directions along the z axis.

the thermal conductivity is calculated from Fourier's law, $J = -\kappa \cdot \mathrm{d}T/\mathrm{d}x$, where J is the heat current, κ is thermal conductivity tensor, and $\mathrm{d}T/\mathrm{d}x$ is the temperature gradient.

In a previous study on silicon, it was shown that the thermal conductivity depends weakly on the cross-sectional area [25]. We have therefore chosen the cross-section of the cylinder 4×4 unit cells, which is the smallest size that can be simulated with the cutoff values used in these potentials of $R_c = 1.9a$, where a is the lattice parameter. The previous studies of Si also showed that the calculated thermal conductivity depends strongly on the length of the simulation box. Using the elementary kinetic theory for a phonon gas, it can be shown that

$$\kappa = \frac{1}{3} c_v v_S l_{\mathrm{eff}}, \tag{8}$$

where c_v is the volumetric specific heat, v_S is the mean sound velocity, and l_{eff} is the effective mean free path of phonons. The appropriate specific heat above the Debye temperature is given by the Dulong–Petit value for a non-interacting gas

$$c_v = (3/2) k_B n, \tag{9}$$

where k_B is the Boltzmann constant, and n is the number density of the ions. For a cubic lattice with N_c atoms in the unit cell, $n = N_c/a^3$. v_S can be estimated by $v_S = (v_L + 2v_T)/3$, where v_L and v_T are the longitudinal and transverse sound velocities. These values are given by $v_L = \sqrt{\rho/C_{11}}$ and $v_T = \sqrt{\rho/C_{44}}$ for a cubic lattice. The effective mean free path can be written as, using Matthiessen's rule for the relaxation time [25] as

$$l_{\mathrm{eff}}^{-1} = l_{\infty}^{-1} + l_{\mathrm{BC}}^{-1}, \tag{10}$$

where l_{∞}^{-1} and l_{BC}^{-1} are the mean free path of phonon–phonon scattering in an infinite media and phonon-boundary scattering, respectively. In our simulation, l_{BC} is approximated by $L_z/4$ since the heat source and sink are separated by $L_z/2$.

Finally the thermal conductivity can be written as a function of system length as

$$\frac{1}{\kappa} = \frac{2a^3}{k_B N_c v_S} \left(\frac{1}{l_{\infty}} + \frac{4}{L_z} \right). \tag{11}$$

This means that the infinite size bulk thermal conductivity is obtained from MD simulations by the extrapolation of the conductivity values to $1/L_z = 0$. This approach was previously applied to Si and diamond single crystals [25].

We have therefore determined the thermal conductivity of single-crystal UO_2 between 300 K and 2000 K as a function of system length. The results for the two potentials are shown in Fig. 3 as $1/\kappa$ vs $1/L_z$ plots, in accordance with Eq. (11). We see that the results for the two potentials are similar at all temperatures and system sizes.

We have determined the thermal conductivity for infinite system size from the linear fits to the data in Fig. 3. These infinite size limit thermal conductivities, which are our best estimates of the intrinsic thermal conductivity of UO_2 described by these potentials, are shown for the two potentials in Fig. 4(a) as a function of temperature. Although the error bars overlap, it does appear that the Yamada potential gives a somewhat higher estimated thermal conductivity at low T than does Busker, but has a somewhat stronger temperature dependence. This result is reasonably consistent with the only small

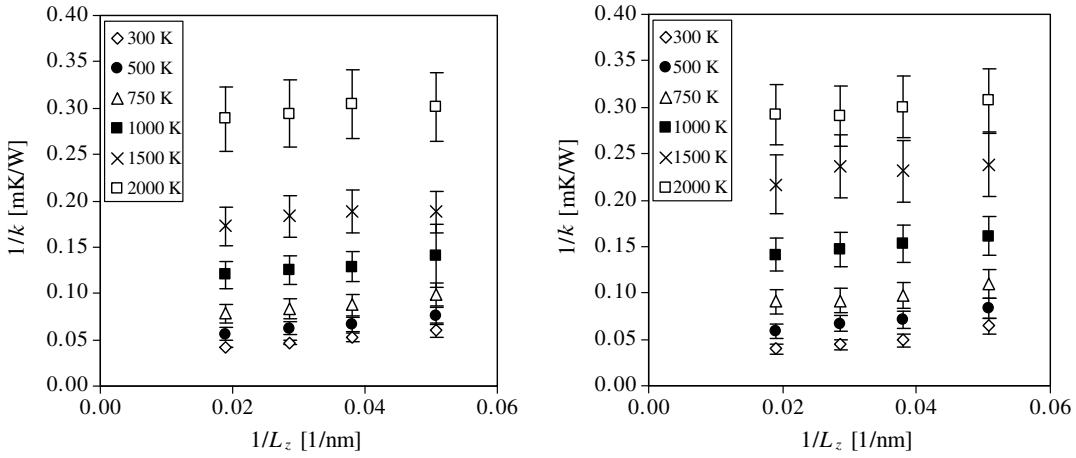

Fig. 3. Size dependence of thermal conductivity for both the Busker (left) and Yamada (right) potentials.

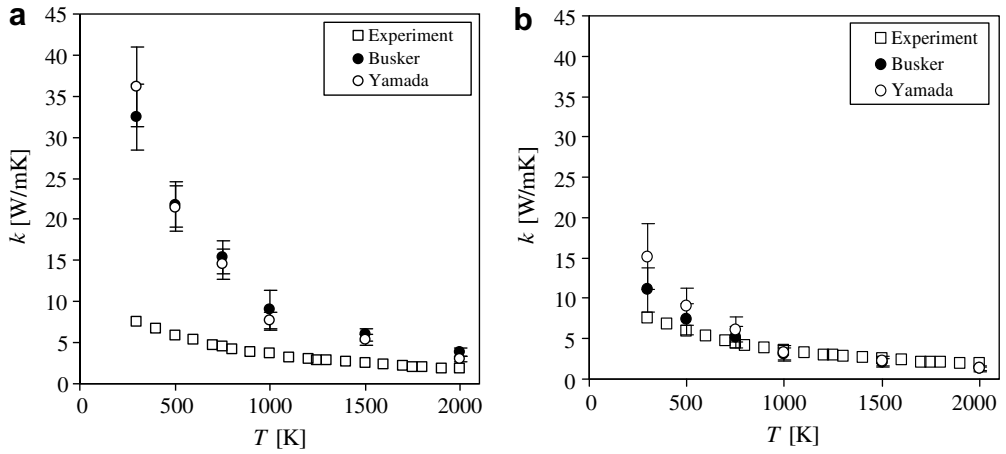

Fig. 4. (a) Thermal conductivity of UO_2 from the compilation of experimental data by Fink and simulations using the Busker and Yamada potentials. (b) The same thermal conductivities with anharmonic correction.

difference in thermal conductivity predicted by our anharmonicity analysis.

The higher values for the estimated thermal conductivity derived using the Yamada potential compared to those previously published for this potential [7] mainly arise from the finite-size effects which are particularly important at low temperatures when the phonon mean-free path is long. A secondary effect is that in this study we have not used the Wigner–Kirkwood correction to the temperature, which has a significant effect below the Debye temperature.

As Fig. 4(a) indicates, both potentials give significantly higher thermal conductivities at low temperatures than the experimental values. Fig. 4(b) shows the thermal conductivity corrected according to the anharmonicity analysis in the previous section; as we can see the match between the simulation and experiment is now much better especially above 750 K, the temperature range of interest for nuclear-fuel applications. It is worth stressing that this agreement is not the result of fitting the simulation results to the experiments, but comes from a physical analysis of the anharmonicity in the experimental and simulated systems, via quantities that are both computationally easy to calculate and generally experimentally available, even for materials in which thermal transport data are lacking. We thus attribute the majority of the difference between the experimental and simulation values as arising from the differences in the bulk modulus for thermal conductivity, which measures the harmonic properties of the system, and the thermal expansion, which measures the anharmonic properties of the system.

The anharmonic Umklapp processes lead to the temperature dependence of the thermal conductivity. Debye showed that $\kappa \sim T^{-n}$, with $n \sim 1$–2 [26]. Fig. 5 is a log–log plot of the data in Fig. 4. In each case, the thermal conductivity shows power-law behavior with temperature. The experimental results are fitted by $n_{\mathrm{Expt}} \sim 0.79$, while the simulations yield $n_{\mathrm{Yamada}} \sim 1.14$ and $n_{\mathrm{Busker}} \sim 1.30$, respectively, which are consistent with the Debye analysis.

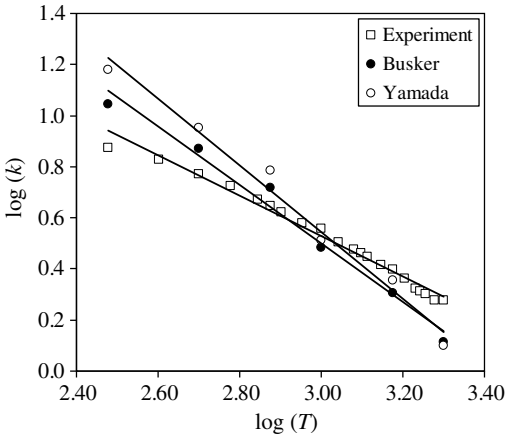

Fig. 5. The same thermal conductivity data as in Fig. 4(b), but in log–log plot.

The systems we have simulated are structurally much simpler than the experimental systems; this also contributes to the discrepancy between the simulation and experimental results. In particular, in the simulations there are no isotopic defects, no off-stoichiometry, and no microstructural defects (grain boundaries, dislocations, second phases etc.) We characterize the effects of polycrystalline microstructures in the next section.

4. Thermal conductivity of polycrystalline UO_2

Grain boundaries offer a significant obstacle to the transport of heat in phonon conductors. In this section, we determine the thermal conductivity of a model fine-grained polycrystal of UO_2, from which we make predictions for the grain-size dependence of its thermal conductivity.

4.1. Structure of model polycrystal

Experimental grain sizes of the range of tens or hundred of microns are not accessible to MD simulation, since each

grain would contain $\sim 10^{13}$–10^{16} ions. We simulate considerably smaller systems with grain sizes from 3.8 to 6.5 nm; these small sizes maximize the area of the grain boundary in the system, thereby amplifying the interfacial effects.

The polycrystalline structures used in the simulations consisted of 24 hexagonal columnar grains. When constructing the polycrystalline structure, identical close-packed hexagons are arranged to form a completely periodic structure. Each hexagon is filled with single-crystal UO_2 oriented with [0 0 1] along the columnar direction. The in-plane orientations are chosen in such a way that the grain boundaries (GBs) between the grains are high energy tilt GBs, which ensures that the microstructure is stable against coarsening during the simulation. Because of the way each grain is constructed, initially there are always a small number of atoms in the GBs which are extremely close to each other. To address this issue, if any two ions are closer than 0.15 nm (66% of the nearest neighbor distance between U^{4+} and O^{2-}, 0.229 nm), one of the atoms is removed. This removal of atoms is carried out with care to ensure the charge neutrality of the entire system. Once the structure is created, it is quenched at 0 K to equilibrate all of the atom positions and to eliminate any in-plane stress on the system. It was found that no ions have anomalously high energies, indicating that the bonding in the system is physically reasonable. The system was then annealed with a constant-pressure, constant-temperature simulation at 2000 K and slowly relaxed to 0 K to ensure that the structure is equilibrated. Fig. 6 shows the final relaxed polycrystalline UO_2 structure for a grain size of 3.8 nm.

The columnar microstructure used here allows the simulation cell to be thin along the columnar direction. The cutoff to the potentials is 1.04 nm, which would allow the thickness to be as small as 4 unit cells: in our simulations, we use 5 unit cells thick so as minimize any effects of the system size in that direction.

Since all the grains are equiaxial and equal size, it is easy to calculate the grain boundary area and volume fraction. For a grain size of 3.8 nm, the area of the GB is 439.10 nm^2. If we assume a unit cell for the thickness of the grain boundary, the volume which the grain boundary region occupies is approximately 30% of the entire volume in both models. The structural disorder at the GBs led to a total volume expansion of 5.5% and 5.3% for Busker and Yamada potentials, respectively. The corresponding GB energies are 2.73 J/m^2 and 1.89 J/m^2, which are consistent with the GB energies of other ceramic materials [27,28].

After the preparation of the equilibrated structure, the thermal expansion of this polycrystalline UO_2 was determined at 300 K. The values obtained were $7.57 \times 10^{-6}\,K^{-1}$ with Busker potential and $8.92 \times 10^{-6}\,K^{-1}$ for Yamada potential, which are almost indistinguishable from the corresponding bulk single crystal values of $7.50 \times 10^{-6}\,K^{-1}$ and $8.83 \times 10^{-6}\,K^{-1}$.

4.2. Thermal conductivity of polycrystalline UO_2

The thermal conductivity of polycrystalline UO_2 is calculated using the direct method described in Section 3. The thermal conductivity of polycrystal has been scaled according to the anharmonic analysis. In this step, we have assumed that the thermal expansion and bulk modulus are essentially microstructure independent. Fig. 7 shows the temperature dependence of κ for a polycrystal with a grain size of 3.8 nm. These calculated thermal conductivities are considerably lower than those from the perfect crystal calculations, attesting to the significant resistance of GB to the flow of heat through the system. Unlike single-crystalline UO_2, finite-size effects are small in polycrystals because the grain boundary scattering dominates over the phonon–phonon scattering. Elsewhere, we have characterized the effect of system size on polycrystalline MgO [29], and shown that the system size dependence is weak. Since UO_2 has significantly lower thermal conductivity than MgO, system-size effects are expected to be even less important.

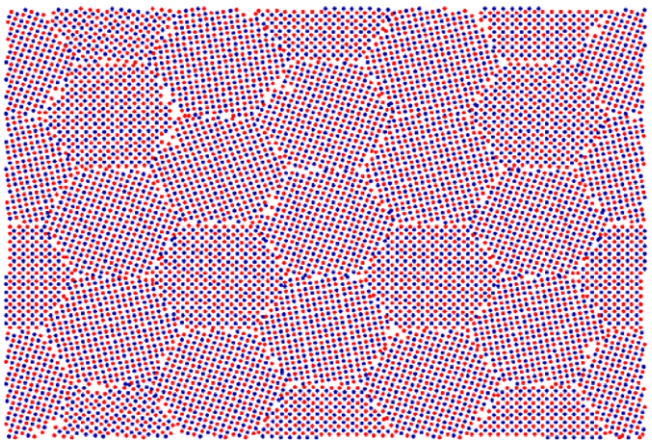

Fig. 6. The final polycrystalline structure used in the thermal conductivity calculations. Blue and red indicate uranium and oxygen ions, respectively. The view is along [0 0 1] in the fluorite crystal structure.

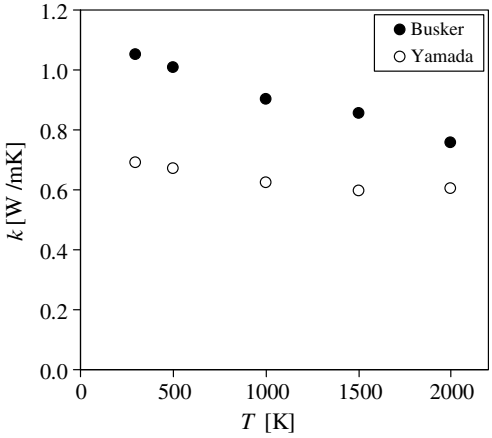

Fig. 7. Thermal conductivity of 3.8 nm grain polycrystalline UO_2 from simulations.

The thermal conductivity for the polycrystal described is considerably higher for the Busker potential than for the Yamada potential. Since the GB energy is a measure of the structural disorder at the interfaces, we expect that the higher the energy associated with the GBs, the higher the interfacial thermal resistance, and the lower the thermal conductivity of the polycrystal. We recall that the GB energies obtained from the Busker and Yamada are 2.73 J/m^2 and 1.89 J/m^2, which appears to be inconsistent with this argument. However, the Busker potential is a full charge model, while the Yamada potential is a partial charge model, resulting in cohesive energies of -104.482 eV/UO_2 and -45.54 eV/UO_2, respectively. Thus, when normalized to the bulk cohesive energies, the GB energies are 0.26 nm^{-2} and 0.16 nm^{-2} for Yamada and Busker, respectively. That is, when described by the Busker potential, the GBs actually offer less of an obstacle to heat transport than for the Yamada potential, which is consistent with the higher thermal conductivity for the Busker potential than for the Yamada potential.

The ensemble-averaged interfacial (Kapitza) resistance of the grain boundaries in the polycrystal can be extracted from the thermal conductivity using a simple model. There are several models proposed, including those of Nan and Birringer [30], Yang et al. [31], and Amrit [32]. For this analysis, we adopt the model by Yang et al. [31] in which the polycrystal is assumed to consist of perfect crystal grains, with conductivities of the perfect crystal, separated by GBs, all of which have the same thermal properties. The interfacial conductance, G_K, is then given by

$$G_K = \frac{1}{d}\frac{\kappa_0 \kappa}{\kappa_0 - \kappa}, \tag{12}$$

where d is the grain size, κ_0 is the single crystal thermal conductivity, and κ is the thermal conductivity of polycrystalline UO_2.

The resulting values of G_K are given in Fig. 8. Both potentials show moderate increase of interfacial conductance with temperature. This temperature increase is consistent with simulation of other interfacial systems [33] and, more importantly, with trends in experimental data for various systems [34]. The physical origin of the increase in conductance with temperature can be understood in terms of the properties of the grain boundaries. As the temperature increases, the anharmonicity of the interactions among the atoms is probed more strongly. While in the perfect crystal, the resulting scattering lowers the thermal conductivity, this anharmonic scattering more strongly couples modes across the interfaces, leading to better interfacial thermal transport.

The interfacial conductance can be recast in terms of the Kapitza length, $l_\kappa = \kappa_0/G_K$, where κ_0 is thermal conductivity of infinite size single-crystal UO_2. The Kapitza length is the thickness of perfect crystal that would offer the same thermal resistance as the interface; thus a long Kapitza length corresponds to a high interfacial resistance. As shown in Fig. 9, the Kapitza length decreases strongly with increasing temperature; this is a result of the decrease in the thermal conductivity and the increase in the interfacial conductance with temperature.

We note that for both potentials, the Kapitza length is significantly larger than the grain diameter particularly in the low temperature region. This is an indication that the thermal transport in our model system is dominated by the GBs. It also suggests that the fundamental assumption of separable and grain-size bulk and interfacial thermal properties used for the analysis may be violated at these small grain sizes.

We have also investigated the effects of grain size on thermal conductivity, for grain sizes up to 6.5 nm grains. The inset to Fig. 10 shows an increase in thermal conductivity with increasing grain size, the result of the decrease in the relative volume of grain boundaries in the system. Our data on for polycrystals simulated with the Yamada potential are fit to the model of Yang et al., thereby allowing the thermal conductivity for large grain sizes to be estimated. Taking the bulk single crystal conductivity of

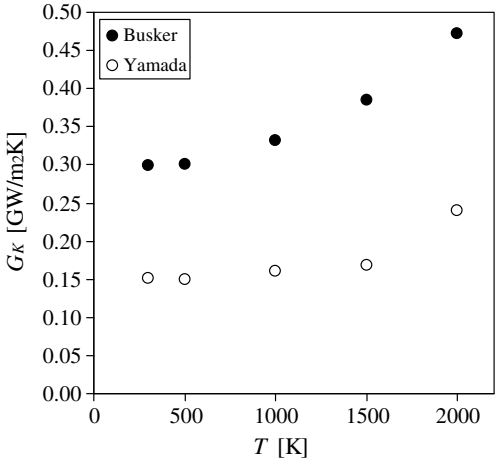

Fig. 8. Thermal conductance of grain boundaries from 3.8 nm grain polycrystalline UO_2 simulations.

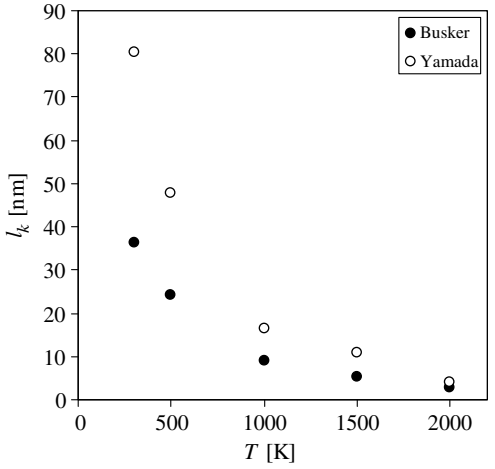

Fig. 9. Kapitza length from 3.8 nm grain polycrystalline UO_2 simulations.

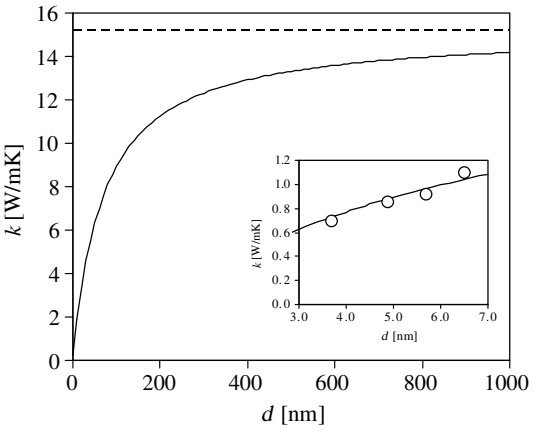

Fig. 10. Grain size dependence of the thermal conductivity of polycrystalline UO_2 using Yamada's model. The solid line is the fit of the model by Yang et al. [31]. Inset is the same plot for nano-meter scale indicating the fit with our data.

15.2 W/m K at 300 K, the fit gives the Kapitza conductance of 0.15 GW/m^2 K, which is close to the value previously determined for the 3.8 nm polycrystal (see Fig. 8).

5. Discussion and conclusions

The simulation approaches used here are well suited to the characterization of the thermal transport properties of electrically insulating materials such as UO_2 in which heat is transported by atomic vibrations. However, even in a relatively poor thermal conductor such as UO_2, finite system size effects can lead to a significant underestimate of the thermal conductivity: the systematic variation in system size coupled with a finite-size scaling analysis does appear to offer a viable method for taking these effects into account.

Finite-size effects seem to be less of a problem in the simulation of the polycrystals, particularly at these small grain sizes, presumably because the phonon mean free path is limited by the grain boundaries, rather than by anharmonic phonon interactions. The analysis of the polycrystal to obtain the interfacial conductance is not unambiguous, since the calculated Kaptiza lengths are larger than the grain sizes. However, the fact that the calculated thermal conductivities of polycrystals of different grains sizes, albeit over the narrow range of 3.8–6.5 nm, can be fit to the Yang et al. model, strongly suggest that its use is not unreasonable. Moreover, since the same analysis is used throughout, we can expect the trends of interfacial conductance with temperature to be reasonable.

Neither potential can quantitatively match the experimental thermal conductivity. Based on the analysis of Govers et al., the two potentials used in the study are of a level of materials fidelity as others in the literature [15]. The simple relationship, Eq. (6), relating the elastic properties, thermal expansion and elastic constants suggests that a potential with correct elastic properties and thermal expansion, should well reproduce the thermal-transport properties. A truly general purpose potential would also need to well reproduce the point defect properties. Govers et al. [15] showed that none of the 21 potentials they examined could satisfactorily reproduce the formation and migration energies. There is thus considerable need potentials which better describe UO_2.

Acknowledgements

We are happy to acknowledge useful discussions with Priyank Shukla. This work was funded by DOE-NERI Award DE-FC07-05ID14649.

References

[1] W.I. Finch, U. S. D. o. t. Interior, U.S. Geological Survey, 2002, pp. 1–18.
[2] C.K. Gupta, Materials in Nuclear Energy Applications, CRC Press, Boca Raton, FL, 1989.
[3] P. Jund, R. Jullien, Phys. Rev. B 59 (1999) 13707.
[4] P.B. Allen, J.L. Feldman, J. Fabian, F. Wooten, Philos. Mag. B 79 (1999) 1715.
[5] P.K. Schelling, S.R. Phillpot, D. Wolf, J. Am. Ceram. Soc. 84 (2001) 1609.
[6] A. Maiti, G.D. Mahan, S.T. Pantelides, Solid State Commun. 102 (1997) 517.
[7] K. Yamada, K. Kurosaki, M. Uno, S. Yamanaka, J. Alloy. Compd. 307 (2000) 10.
[8] M. Abramowski, R.W. Grimes, S. Owens, J. Nucl. Mater. 275 (1999) 12.
[9] G. Busker, Ph.D Thesis, Imperial College of Science, Technology, and Medicine, 2002.
[10] Y. Ida, Phys. Earth Planet. Inter. 13 (1976) 97.
[11] M.P. Allen, D.J. Tildesley, Computer Simulation of Liquids, Oxford University, 1987.
[12] D. Wolf, P. Keblinski, S.R. Phillpot, J. Eggebrecht, J. Chem. Phys. 110 (1999) 8254.
[13] J.D. Gale, J. Chemical Society, Faraday Trans. 93 (1997) 629.
[14] J.D. Gale, A.L. Rohl, Mol. Simulat. 29 (2003) 291.
[15] K. Govers, S. Lemehov, M. Verwerft, J. Nucl. Mater. 266 (2007) 161.
[16] H.C. Andersen, J. Chem. Phys. 72 (1980) 2384.
[17] J.K. Fink, J. Nucl. Mater. 279 (2000) 1.
[18] N.W. Ashcroft, D.N. Mermin, Solid State Physics, Saunders College Publishing, 1976.
[19] C. Kittel, Introduction to Solid State Physics, John Wiley, 1996.
[20] J.M. Ziman, Electrons and Phonons, The International Series of Monographs on Physics, Oxford University, London, UK, 1960.
[21] G. Leibfried, E. Schloemann, Math. Phys. K1 IIa (1954) 71.
[22] P.G. Klemens, Solid State Physics 7 (1954) 1.
[23] B.T.M. Willis, Proc. R. Soc. London, Ser. A 274 (1963) 134.
[24] C. Ronchi, M. Sheindlin, M. Musella, G.J. Hyland, J. Appl. Phys. 85 (1999) 776.
[25] P.K. Schelling, S.R. Phillpot, P. Keblinski, Phys. Rev. B 65 (2002), Article No. 144306.
[26] G.H. Geiger, D.R. Poirier, Transport Phenomena in Metallurgy, Addison-Wesley, 1973.
[27] H. Yoshida, K. Yokoyama, N. Shibata, Y. Ikuhara, T. Sakuma, Acta Mater. 52 (2004) 2349.
[28] P. Keblinski, D. Wolf, S.R. Phillpot, H. Gleiter, J. Mater. Res. 13 (1998) 2077.
[29] P. Shukla, T. Watanabe, J.C. Nino, J.S. Tulenko, S.R. Phillpot, J. Nucl. Mater. submitted for publication.
[30] C.W. Nan, R. Birringer, Phys. Rev. B 57 (1998) 8264.
[31] H.S. Yang, G.R. Bai, L.J. Thompson, J.A. Eastman, Acta Mater. 50 (2002) 2309.

[32] J. Amrit, J. Phys. D Appl. Phys. 39 (2006) 4472.
[33] R.J. Stevens, L.V. Zhigilei, P.M. Norris, Int. J. Heat Mass Transfer 50 (2007) 3977.
[34] D.G. Cahill, W.K. Ford, K.E. Goodson, G.D. Mahan, A. Majumdar, H.J. Maris, R. Merlin, S.R. Phillpot, J. Appl. Phys. 93 (2003) 793.
[35] J.B. Wachtman, M.L. Wheat, H.J. Anderson, J.L. Bates, J. Nucl. Mater. 16 (1965) 39.
[36] I.J. Fritz, J. Appl. Phys. 47 (1976) 4353.
[37] D.G. Martin, J. Nucl. Mater. 152 (1988) 94.
[38] G. Dolling, R.A. Cowley, A.D.B. Woods, Can. J. Phys. 43 (1965) 1397.